

## Article

# Materials Based on Amorphous Al<sub>2</sub>O<sub>3</sub> and Composite W-Al<sub>2</sub>O<sub>3</sub> for Solar Coatings Deposited by High-Rate Sputter Processes

Claudia Diletto <sup>1,\*</sup>, Antonio D'Angelo <sup>1</sup>, Salvatore Esposito <sup>1</sup>, Antonio Guglielmo <sup>1</sup>, Daniele Mirabile Gattia <sup>2</sup> and Michela Lanchi <sup>2</sup>

<sup>1</sup> Portici Research Centre, ENEA, P.le E. Fermi 1, 80055 Naples, Italy

<sup>2</sup> Casaccia Research Centre, ENEA, Via Anguillarese 301, 00123 Rome, Italy

\* Correspondence: claudia.diletto@enea.it; Tel.: +39-081-77-23-378

**Abstract:** In parabolic trough technology, the development of thermally and structurally stable solar coatings plays a key role in determining the efficiency, durability, and economic feasibility of tube receivers. A cermet-based solar coating is typically constituted by a thin film stratification, where a multilayer graded cermet is placed between an infrared metallic reflector and an antireflection filter. This work reports the realization of materials based on Al<sub>2</sub>O<sub>3</sub> and W characterized by high structural and chemical stability in vacuum at high temperature, obtained through the optimization of high-deposition-rate processes. Al<sub>2</sub>O<sub>3</sub> material, employed as the antireflection layer, was deposited through a reactive magnetron sputtering process at a high deposition rate. Cermet materials based on W-Al<sub>2</sub>O<sub>3</sub> were deposited and employed as absorber layers by implementing reactive magnetron co-sputtering processes. An investigation into the stability of the realized samples was carried out by means of several material characterization methods before and after the annealing process in vacuum ( $1 \times 10^{-3}$  Pa) at high temperature (620 °C). The structural properties of the samples were evaluated using Raman spectroscopy and XRD measurements, revealing a negligible presence of oxides that can compromise the structural stability. Spectrophotometric analysis showed little variations between the deposited and annealed samples, clearly indicating the high structural stability.

**Keywords:** solar absorber; cermet; reactive sputtering; deposition rate; structural stability



**Citation:** Diletto, C.; D'Angelo, A.; Esposito, S.; Guglielmo, A.; Mirabile Gattia, D.; Lanchi, M. Materials Based on Amorphous Al<sub>2</sub>O<sub>3</sub> and Composite W-Al<sub>2</sub>O<sub>3</sub> for Solar Coatings Deposited by High-Rate Sputter Processes. *Solar* **2023**, *3*, 113–131. <https://doi.org/10.3390/solar3010009>

Academic Editor: Sungwoo Yang

Received: 16 December 2022

Revised: 23 January 2023

Accepted: 31 January 2023

Published: 6 February 2023



**Copyright:** © 2023 by the authors. Licensee MDPI, Basel, Switzerland. This article is an open access article distributed under the terms and conditions of the Creative Commons Attribution (CC BY) license (<https://creativecommons.org/licenses/by/4.0/>).

## 1. Introduction

Receiver tubes used in Concentrating Solar Technology (CST) are components with high technological content. In particular, spectrally selective coatings deposited on receiver tubes by vacuum techniques are a strategic element because they affect the receiver photo-thermal efficiency in terms of solar radiation absorbance ( $\alpha_s$ ) and thermal emittance ( $\epsilon_{th}$ ) [1–3]. Typically, solar coatings characterized by a particular multilayer structure, which consists of one or more cermet layers (optical absorber materials) placed between a metallic layer (infrared reflector) and a ceramic layer (antireflection layer), are used in this specific application. In this structure, every single layer performs a specific function: the metallic layer, with its high optical reflectivity in the infrared region, ensures a low emittance value; the cermet layers, constituted by ceramic/metallic composite materials, absorb incoming solar radiation; lastly, the antireflection layer minimizes reflection losses.

In a vacuum receiver tube for high temperature applications (e.g., with molten salts as heat transfer fluid), the solar coating has to work at a pressure  $\leq 1 \times 10^{-2}$  Pa and up to 550 °C. Under these operating conditions, the constituent materials of the coating should have high structural, physical, and chemical stability to maintain the good performance of the spectrally selective coating [3,4]. In fact, a good selective absorber should not only possess a high solar absorbance and a low thermal emittance but should also be able to retain its properties under long-term operations. Therefore, the development of cermet materials that can prevent any diffusive phenomena and are stable at the operating conditions of receiver

tubes is a relevant objective.  $\text{Al}_2\text{O}_3$ -based cermet coatings, which have excellent optical properties and thermal stability, have been extensively investigated as spectrally selective absorbers [5–10]. Furthermore, some studies report that cermet materials based on tungsten and alumina ( $\text{W-Al}_2\text{O}_3$ ) are suitable for use as absorber layers within spectrally selective coatings, owing to their high chemical and structural stability at high temperatures [11–13]. Particularly, alumina oxide ( $\text{Al}_2\text{O}_3$ ) is a hard compound adopted for wear and corrosion protection due to its excellent properties such as chemical inertness, high hot hardness, and stability at elevated temperature [14,15]. The optical properties of alumina oxide, such as its transparency, coupled with good barrier properties, make it particularly suitable for these applications. Tungsten (W) is a metal with relatively good oxidation resistance and a high melting temperature.

Since 2001, the Italian National Agency for New Technologies, Energy and Sustainable Development (ENEA) has been involved in research devoted to the fabrication of solar coatings for high-temperature parabolic trough receivers using molten salts as heat transfer fluid (550 °C), with the aim of increasing the operative temperature of the solar field and, consequently, the overall plant efficiency [11]. In particular, the research has focused on the realization of stable and efficient materials produced through high-rate deposition processes, easily transferable to the industry, and has led to a patent [16] whose license has been acquired by a national industry in the sector [17].

Initially, the experimental activities were aimed at the production of alumina by a radio frequency (RF) sputtering technique, which is the most reliable process for producing alumina with good repeatability [11]. However, this technique is characterized by a low deposition rate that limits its industrial application.

Among the different techniques to produce ceramic materials with high deposition rates, reactive magnetron sputtering is the most interesting process [18–23]. In particular, the process can be performed by adopting two different regimes, known as transition and poisoned mode [20,24]. The latter is characterized by a low deposition rate and was largely used in the past. Although the deposition processes in poisoned mode are repeatable and robust in terms of plasma instability, they do not permit high deposition rates of ceramic materials, thus limiting the deposition efficiency and economic feasibility of coatings. To overcome these limits, reactive magnetron sputtering in transition mode can be employed. This process allows for higher deposition rates of ceramic materials by more than one order of magnitude [19], which is highly advantageous from an industrial perspective if combined with the possibility of preserving the stability and repeatability of the production process. Indeed, in this process the target conditions are very sensitive to the quantity of reactive gas injected into the process chamber, thus requiring an accurate control of the sputtering process to maintain stable deposition conditions during the ceramic growth [20]. Regarding the realization of cermet materials through reactive magnetron co-sputtering technique in transition mode, the corresponding literature is very poor. In fact, most studies deal with the fabrication of these materials by adopting easier experimental conditions, such as reactive co-sputtering in poisoned mode or RF sputtering techniques [12,25], than reactive magnetron co-sputtering technique in transition mode; besides, there are few existing studies related to the processes performed in transition mode. Moreover, despite the high deposition rate, most of these studies concern the realization of cermet materials based on nitrides [26–29] rather than oxides.

The present work deals with the realization of ceramic materials characterized by high structural and chemical stability at high temperature, obtained through the optimization of a high-deposition-rate process. The employed technique is the “dual magnetron” reactive sputtering in transition mode with medium frequency (MF) supply. Plasma conditions were monitored by a Plasma Emission Monitoring (PEM) system. The optimized materials were employed both as an antireflective layer and ceramic component inside the optical absorber layer. This study also reports the realization of cermet materials based on tungsten and alumina, obtained through the optimization of reactive magnetron co-sputtering technique in transition mode, which is the process for depositing ceramic and metallic components

concurrently. In particular, “dual magnetron” reactive sputtering in transition mode with MF supply was employed to deposit the ceramic component ( $\text{Al}_2\text{O}_3$ ), while “standard magnetron” reactive sputtering with impulsive direct current (DC) supply was employed to deposit the metallic component (W).

The realized materials were subjected to optical and structural characterizations and thermal annealing tests in vacuum ( $1 \times 10^{-3}$  Pa) at high temperature ( $620^\circ\text{C}$ ) to verify their stability and define the most suitable process conditions for the fabrication of materials with the required characteristics. The possible material degradation was investigated by several characterization techniques: UV-Vis-NIR spectrophotometric analysis, X-ray Diffraction analysis (XRD), and Raman spectroscopy.

## 2. Experimental Section

### 2.1. Magnetron Sputtering System

Ceramic and cermet films of the spectrally selective solar coatings were deposited by magnetron sputtering technique using a prototypical sputtering system composed of a load-lock chamber and a process chamber. This plant has a vertical general layout and allows samples to oscillate by moving back and forth from the sputtering source. Figure 1 shows the general view of the cited sputtering plant. Typically, plasma etching and heating pre-treatments are performed on substrates in the load-lock chamber. In the process chamber, six cathodes, namely three standard magnetron cathodes, used to deposit metallic materials, and three dual magnetron cathodes, used to deposit ceramic oxides, were mounted and arranged in pairs on two opposite sides. The simultaneous deposition of metallic and ceramic materials by co-sputtering technique allows one to obtain cermet materials.



**Figure 1.** A general view of ENEA-2 sputtering plant.

In this work, a tungsten target mounted on a standard magnetron cathode provided the metallic component while two aluminum targets mounted on a dual magnetron cathode provided the ceramic component. The deposition plant was also equipped with a PEM system (PLASUS, GmbH Company equipment, Mering, Germany) characterized by six independent spectrometric channels. The complete spectrum of the plasma light emission was acquired continuously by optical fibers in the wavelength range 200–1100 nm. Each dual magnetron cathode was monitored by two optical fibers, one fiber for each plasma region facing the two targets of the dual magnetron cathode. The control system with PEM

used very fast feedback to ensure a stable sputtering at a selected value of reference signal (corresponding to the desired set-point). This control function was performed through a proportional-integral-derivative (PID) controller, which allows one to maintain the target conditions during the reactive sputtering process.

## 2.2. Materials Preparation

Ceramic and cermet films were deposited on glass, stainless steel (SS) (nominal dimensions of both substrates were 26 mm × 75 mm × 1.1 mm), and on monocrystalline Silicon (c-Si) planar substrates fixed inside housing on the external surface of an SS tube (L = 600 mm, D = 70 mm). This tube holder moves back and forth with respect to the targets with adjustable sweep velocity and rotates with an adjustable spin velocity. Sweep and spin velocities were properly chosen to have a good plasma stability during processes and were fixed at 250 mm/min and 60 rpm, respectively.

Ceramic and cermet materials were deposited by reactive sputtering under an oxygen and argon atmosphere. The ultimate pressure before starting deposition processes was  $7 \times 10^{-5}$  Pa, obtained by using a cryogenic pump system.

Al<sub>2</sub>O<sub>3</sub> ceramic deposition was performed by applying a power density to Al targets equal to 1.84 W/cm<sup>2</sup>. The process pressure was fixed at about 1 Pa by introducing a total Ar flow equal to 400 sccm through the gas rings placed around the frontal Al and W targets (200 sccm for side) to maintain the same gas flow configuration as the W-Al<sub>2</sub>O<sub>3</sub> cermet deposition (described momentarily). The oxygen flow was introduced into the process chamber from the gas rings around the Al targets and was controlled by the PEM system. Before each deposition, two pre-sputtering phases were performed: in the first phase, only Ar gas was introduced into the process chamber, in order to clean the Al targets; in the second phase, oxygen reactive gas was also injected so that the selected spectral response of the plasma was effected. These two steps allowed for the deposition of alumina thin films through the Al targets with the same starting conditions, which could then be monitored through voltage and current values.

Regarding the cermet materials, different samples were deposited by applying a constant power density to the Al targets, equal to 1.84 W/cm<sup>2</sup>, and variable cathode power densities to the W target (positioned in opposite side, co-sputtering mode), equal to 9.78, 6.67, 3.56, and 1.33 W/cm<sup>2</sup>. The process pressure was fixed at about 1 Pa by introducing a total Ar flow equal to 400 sccm through the gas rings placed around the frontal Al and W targets (200 sccm per side). An oxygen gas flow was introduced into the process chamber from the gas rings around the Al targets and was controlled by the PEM system.

## 2.3. Materials Characterization

Optical reflectance and transmittance measurements of the realized samples were carried out using a UV-Vis-NIR spectrophotometer mod. Lambda 950 (Perkin-Elmer Company, Waltham, Massachusetts) equipped with a double beam and a 15 cm diameter integrating sphere.

The thickness of each ceramic and cermet layer was mechanically measured on films grown on glass substrate using a Tencor P-7 stylus profiler, (KLA Company, Milpitas, California). A shadow mask was applied to the substrate before the deposition and removed after the process. This procedure allowed for the creation of a step used to evaluate the thickness of the realized samples.

X-ray diffraction analysis was performed using a Smartlab diffractometer (Rigaku Company, The Woodlands, Texas) working with CuK $\alpha$  radiation ( $\lambda = 1.54059$  nm). The glancing incidence configuration was used to obtain high sensitivity to the film structure: different measurements were collected at decreasing incidence angles, starting from 3.5° on the cermet layers deposited on both glass and c-Si substrates. A scan range of 10–90° (2 $\theta$ ) was used.

The Raman measurements were acquired at ambient conditions with a Renishaw Raman microscope, using the 514 nm excitation of a green laser. An acquisition time

of 10 s for each spectrum and a  $50\times$  objective lens were used in all experiments. These characterizations were performed on samples deposited on c-Si substrates.

Thermal annealing cycles were carried out by a Carbolite programmable furnace operating in vacuum at a pressure of  $1.0 \times 10^{-3}$  Pa and temperature equal to  $620^\circ\text{C}$ . Thermal annealing tests were conducted for a total of 132 days according to the following six cycles: first cycle of 2 days, second cycle of 7 days, third cycle of 10 days, fourth cycle of 18 days, fifth cycle of 37 days, and sixth cycle of 58 days. At the end of each cycle, optical and structural characteristics were verified to evaluate the thermal stability of the realized samples. Figure 2 shows a diagram with detailed descriptions of all the steps involved to realize and characterize the samples discussed.

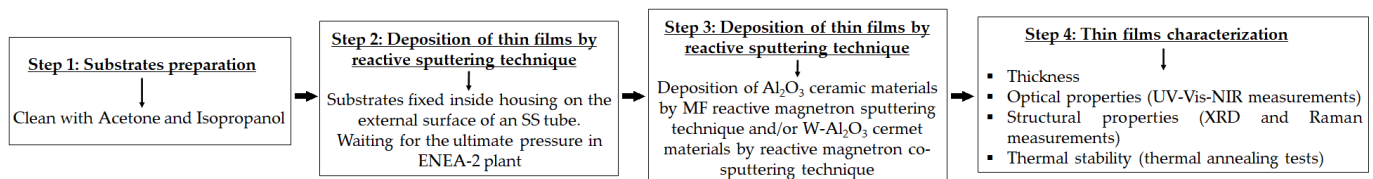


**Figure 2.** Diagram with detailed descriptions of all the steps involved to realize and characterize the samples.

### 3. Results and Discussion

The experimental work described in this article concerns the optimization of a high-deposition-rate, high-reproducibility process for the realization of ceramic and cermet materials characterized by high structural and chemical stability in vacuum at high temperature. The implemented technique was reactive magnetron sputtering in transition mode.

#### 3.1. Alumina

Alumina is the material used both as an antireflection layer and a ceramic component of cermet. Suitable process parameters were identified and optimized to deposit a ceramic material with the required optical characteristics, namely a non-absorbent ceramic material at wavelength values above 500 nm.

Alumina thin film deposition was carried out through the preliminary acquisition of the hysteresis curve to individuate the transition region. Figure 3 shows the hysteresis curve of the process performed at a power density of  $1.84\text{ W/cm}^2$  applied to the Al targets.

The shape of this curve depends on several factors such as power density, process pressure, and gas flow introduced into the chamber. One way to eliminate the hysteresis effect is to “overpump” the deposition chamber by using a pumping system with a pumping speed that is sufficiently high so that the consumption of the reactive gas by the pumping system dominates that of the growing film on the target surface [20,24,30]. As a result, a gradual transition from metallic to poisoned modes takes place. For this reason, alumina depositions were carried out by high Ar flow (400 sccm) to obtain high pumping speed.

The “response curve” reported in Figure 3 was obtained by increasing and decreasing the oxygen flow injected into the process chamber. The intensity of the emission spectral line of aluminum (Counts, Cts) was measured for each value of reactive gas flow. The reactive gas flow was tuned through the variation of voltage applied to the opening valve of the mass flow controller. It is worth noting that the intensity of the emission spectral lines of aluminum or oxygen could be monitored during this deposition, since both elements were present in the plasma. However, the oxygen had more excited states, with emission spectral lines that were not very intense. Conversely, the intensity of the emission spectral line of aluminum was very high and very sensitive to the reactive gas flow variations inside the chamber.

The working point of the depositions was established through the “response curve” analysis: the intensity of the emission spectral line of Al, kept constant during the process, was selected. This value corresponds to the voltage value used by the PEM to inject the oxygen flow required to obtain the ceramic material with the desired optical characteristics.

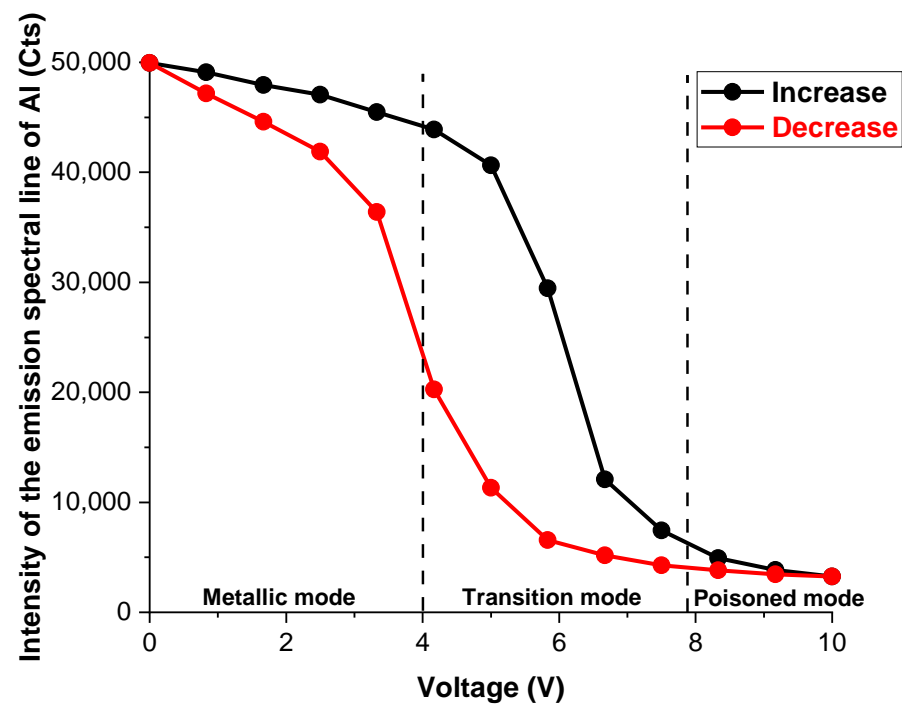


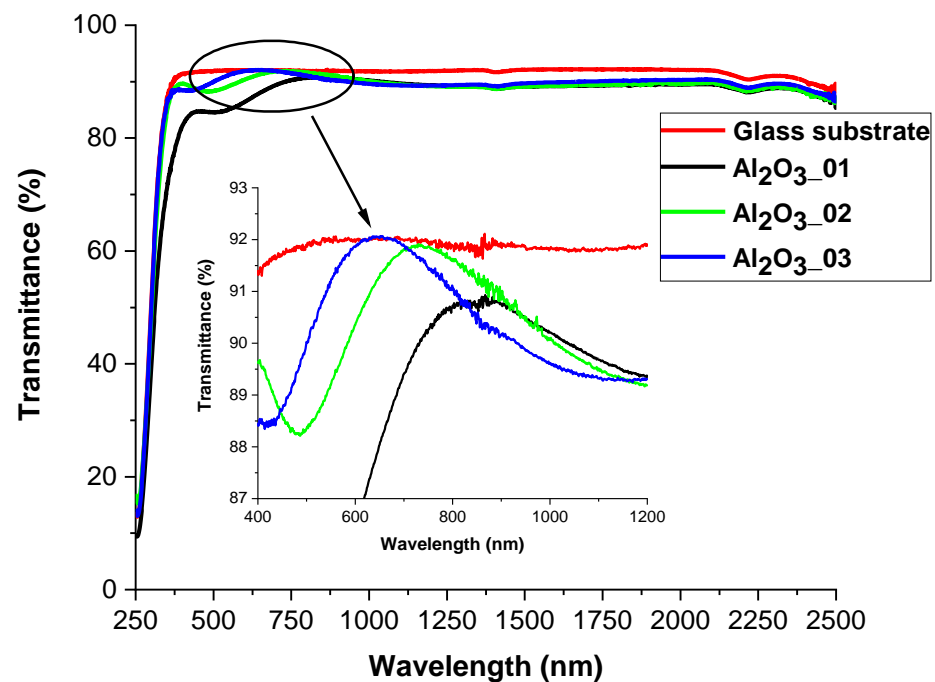
**Figure 3.** Hysteresis curve of the aluminum targets obtained at  $1.84 \text{ W/cm}^2$  by monitoring the intensity of the emission spectral line of Al as a function of the voltage value used by the PEM to inject the oxygen flow.

Before starting alumina deposition, a process simulation was carried out by moving the tube holder back and forth with respect to the Al targets to evaluate the influence of this movement on the stability of the selected intensity. In fact, the tube holder's movement can cause a variation of plasma distribution that can be very significant if it is combined with high sweep velocity. As can be seen from Figure 3, the curve's slope is very high in the transition zone, and the hysteresis curve can suddenly move into the metallic or poisoned region due to small reactive gas flow variations. This represents the main issue with this kind of process. The working point should not move into the metallic or poisoned region, because the resulting ceramic material might present altered optical properties. The process simulation allowed for the identification of both sweep and spin velocities, which led to a well-controlled intensity of the emission spectral line of aluminum. The corresponding values are reported in the Section 2. Hence, various alumina samples were deposited using the process parameters reported in Table 1. It should be noted that three different intensities of the emission spectral line of aluminum were selected to identify the optimal reactive gas flow into the PEM system and obtain the required ceramic, not absorbent, material. The choice of the correct intensity of the emission spectral line of aluminum, and thus of the optimal oxygen flow controlled by the PEM, is the key parameter to optimize  $\text{Al}_2\text{O}_3$  deposition.

The fabricated samples were named  $\text{Al}_2\text{O}_3_{01}$ ,  $\text{Al}_2\text{O}_3_{02}$ , and  $\text{Al}_2\text{O}_3_{03}$ ; their thicknesses were equal to 238 nm, 213 nm, and 197 nm, respectively. Figure 4 shows the corresponding transmittance curves compared to that of glass substrate used for the deposit. This figure shows that low-oxygen quantities injected into the process chamber have the simultaneous effect of increasing the deposition rate (the corresponding values are reported in Table 1) and the metallic aluminum percentage inside the thin film. This phenomenon is clearly visible for the sample  $\text{Al}_2\text{O}_3_{01}$ , which shows a significant absorption due to the presence of metallic aluminum inside the structure. For this reason, the maximum points of the interference fringes are very far away from the transmittance curve of glass substrate, as shown in the inset of Figure 4.

**Table 1.** Process parameters used to deposit Al<sub>2</sub>O<sub>3</sub> samples.

Process Parameters	Al <sub>2</sub> O <sub>3</sub> _01	Al <sub>2</sub> O <sub>3</sub> _02	Al <sub>2</sub> O <sub>3</sub> _03
Argon flow (sccm)	400	400	400
Oxygen flow (sccm)	5	5.4	5.6
Process pressure (Pa)	~1	~1	~1
Al power density (W/cm <sup>2</sup> )	1.84	1.84	1.84
Intensity of emission spectral line of Al (Cts)	40,000	38,000	36,000
Deposition rate (Å/s)	0.79	0.71	0.66

**Figure 4.** Comparison between the transmittance curves of glass substrate and Al<sub>2</sub>O<sub>3</sub> samples deposited by varying the intensity of the emission spectral line of aluminum.

Samples deposited using higher oxygen quantities than the Al<sub>2</sub>O<sub>3</sub>\_01 sample are characterized by different optical behavior. Al<sub>2</sub>O<sub>3</sub>\_02 thin film has interference fringes that are almost tangent to the transmittance curve of glass substrate around 800 nm; conversely, the Al<sub>2</sub>O<sub>3</sub>\_03 sample has interference fringes that are tangent to the transmittance curve of glass substrate around 600 nm. This indicates the non-absorbent properties of these alumina thin films over 800 nm and 600 nm, respectively, and the possibility to obtain the ceramic material with the required optical characteristics in both cases.

In order to evaluate the reproducibility of sputtering process in transition mode, a further alumina sample named Al<sub>2</sub>O<sub>3</sub>\_04 was deposited by adopting the same experimental conditions as the Al<sub>2</sub>O<sub>3</sub>\_02 sample, which is the thin film produced at the highest sputtering rate and has the required optical characteristics. The deposition rate obtained for Al<sub>2</sub>O<sub>3</sub>\_04 was equal to 0.73 Å/s; the comparison between the transmittance curves of these two samples is shown in Figure 5. The good overlap of the transmittance curves, together with the equal deposition rate values, clearly demonstrates the excellent reproducibility of the implemented reactive sputtering process in transition mode.

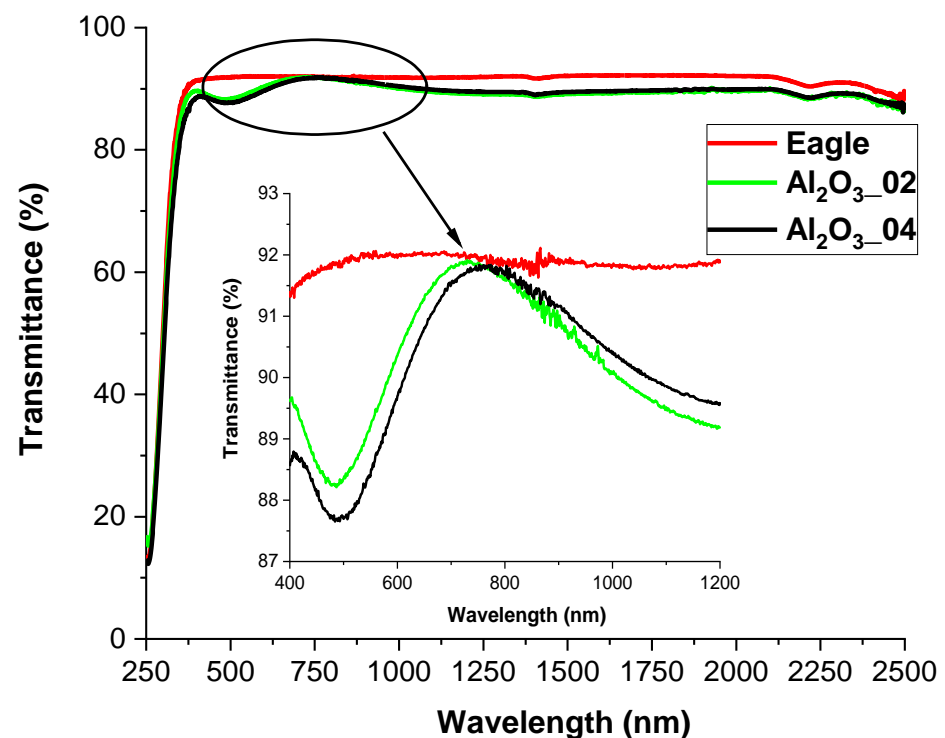


**Figure 5.** Comparison between the transmittance curves of glass substrate and  $\text{Al}_2\text{O}_3$  samples deposited in the same experimental conditions.

Lastly, deposition rates between two reactive sputtering processes performed in transition and poisoned regimes were compared by realizing two samples with the same deposition conditions, except for the reactive gas flow injected into the process chamber. The deposition rate obtained for the transition mode was about sixteen times higher than that of the poisoned mode.

### 3.2. $\text{W-Al}_2\text{O}_3$ Cermet

Cermet materials based on tungsten and alumina were deposited and employed as absorber layers within solar coatings. Ceramic and metallic components were concurrently deposited through the reactive co-sputtering technique in the transition regime. In order to promote  $\text{W-Al}_2\text{O}_3$  cermet growth and avoid a possible oxidation of its metallic component, the reactive gas was only introduced through gas rings placed around the Al targets.

A possible oxidation of the metallic components can reduce the absorption properties of realized cermet; consequently, thicker layers or cermet with higher metallic content are necessary to obtain the same absorption characteristics as those of the non-oxidized one. Moreover, these metallic oxides (e.g., tungsten oxide) can be volatile compounds at the operative conditions of tube receivers. Several authors have studied the kinetics of oxidation of pure tungsten [31,32]: they report that the volatile oxide of tungsten is  $\text{WO}_3$ , which can be directly produced from the solid phase of  $\text{WO}_3$  or from the transmutation process of the solid phase  $\text{WO}_2$  [31]. The presence of this volatile oxide within the absorber layer can damage the structural stability of cermet. For these reasons, only the deposition technique and the relative process parameters which minimize the formation of these volatile compounds need to be considered here. The reactive magnetron sputtering in transition mode can be effectively applied for the scope, since it requests the least possible amount of reactive gas to promote ceramic component growth.

Cermet depositions initially required the preliminary acquisition of hysteresis curves to individuate the working points of the processes. In this case, the process setup was particularly complex due to the interference between the plasma regions facing the W and Al targets. Different hysteresis curves were acquired, depending on the power density applied to the W target; in fact, to realize cermet materials with different metallic content, a fixed power density (equal to the power density used to deposit alumina samples) applied to the Al targets and variable cathode power densities applied to the W target were used. In this process, the ceramic components of all cermet materials were deposited with the same voltage at the Al targets; this reference voltage was then used to detect the working point for the ceramic component deposition of each cermet material. This ensured that the surface conditions at the aluminum target were always the same, both when the tungsten target was off and on at the different power supplies. The experimental procedure involved three phases: (i) acquisition of the hysteresis curves; (ii) choice of the working points; and (iii) processes simulation, thus adopting the same operating procedure employed for the ceramic deposition. Table 2 shows the process parameters and the thickness evaluations of the four cermet samples: W-Al<sub>2</sub>O<sub>3</sub>\_01, W-Al<sub>2</sub>O<sub>3</sub>\_02, W-Al<sub>2</sub>O<sub>3</sub>\_03, and W-Al<sub>2</sub>O<sub>3</sub>\_04. Figure 6a,b show their transmittance and reflectance curves, respectively.

**Table 2.** Process parameters and thickness evaluations for cermet samples obtained by varying the power density applied to the W target and keeping a fixed power density applied to the Al targets.

Process Parameters	W-Al <sub>2</sub> O <sub>3</sub> _01	W-Al <sub>2</sub> O <sub>3</sub> _02	W-Al <sub>2</sub> O <sub>3</sub> _03	W-Al <sub>2</sub> O <sub>3</sub> _04
Argon flow (sccm)	400	400	400	400
Oxygen flow (sccm)	5.8	5.6	5.5	5.4
Process pressure (Pa)	~1	~1	~1	~1
Al power density (W/cm <sup>2</sup> )	1.84	1.84	1.84	1.84
W power density (W/cm <sup>2</sup> )	9.78	6.67	3.56	1.33
Intensity of emission spectral line of Al (Cts)	30,000	35,000	35,000	35,000
Thickness (Å/s)	508	421	299	395

The refractive index (n) and extinction coefficient (k) were estimated using an inversion method applied to the experimental reflectance and transmittance data [33]. Their trends as a function of wavelength are reported in Figure 7a,b, respectively. The curves demonstrate the effective possibility of realizing cermet samples with a strongly variable extinction coefficient as a function of power density applied to the metallic target. This property of cermet, coupled with the achievement of suitable thicknesses of absorber layers, is very useful for realizing a solar absorber with a graded metallic profile, namely cermet layers in which the metallic content decreases from infrared back reflector to antireflection filter. This type of structure ensures good absorption of incoming solar radiation. Clearly, the process here, when optimized, allows for the realization of cermet materials with globally high deposition rates, since the metallic component is intrinsically deposited at a high rate, while the ceramic component is deposited by reactive magnetron sputtering in transition mode that also ensures a high deposition rate, as previously mentioned. This represents the main advantage of this kind of process, although its application on an industrial scale [34] is possible but very difficult since even a slight change in setup can result in a large change in deposition rates and composition.

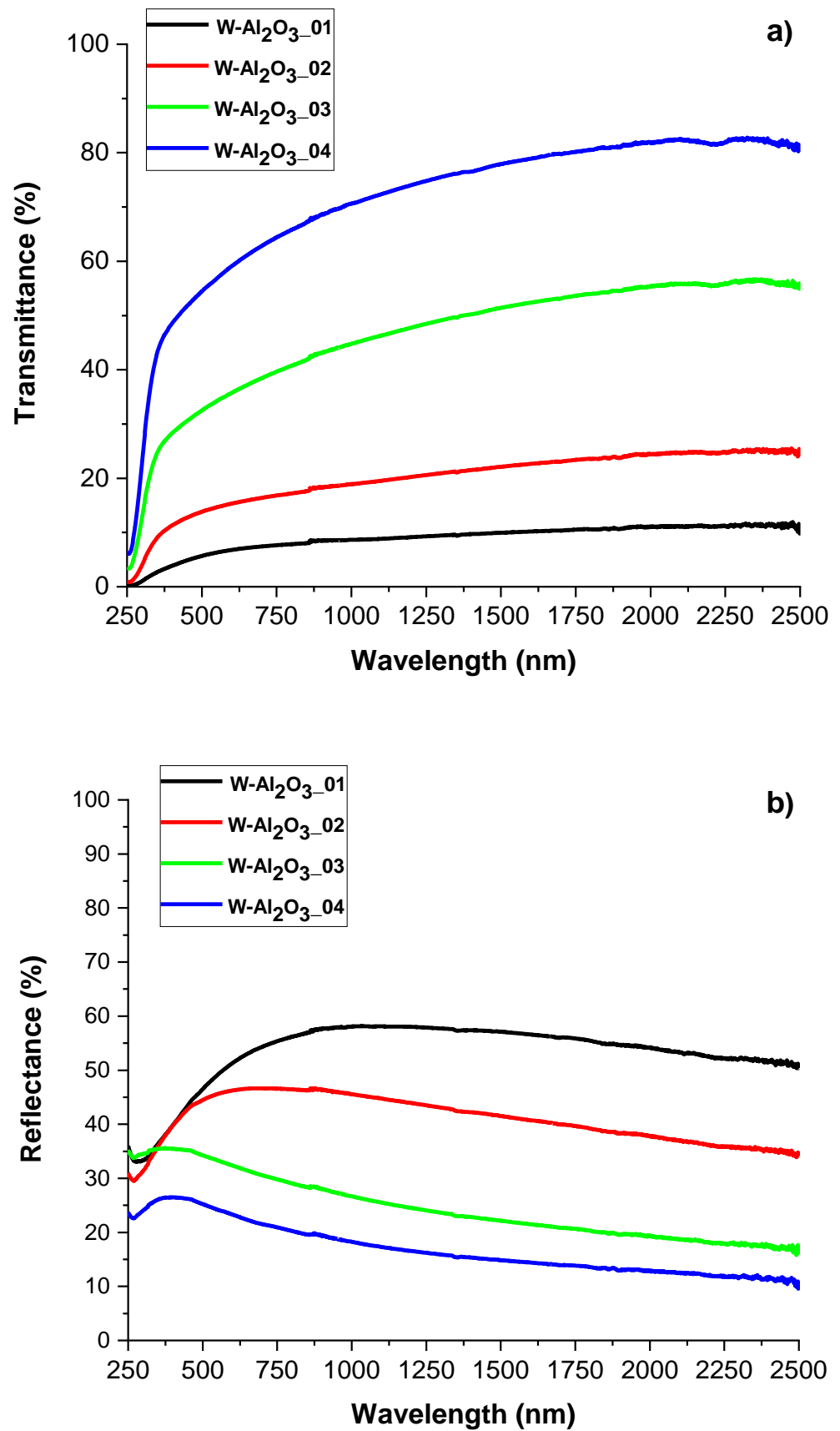
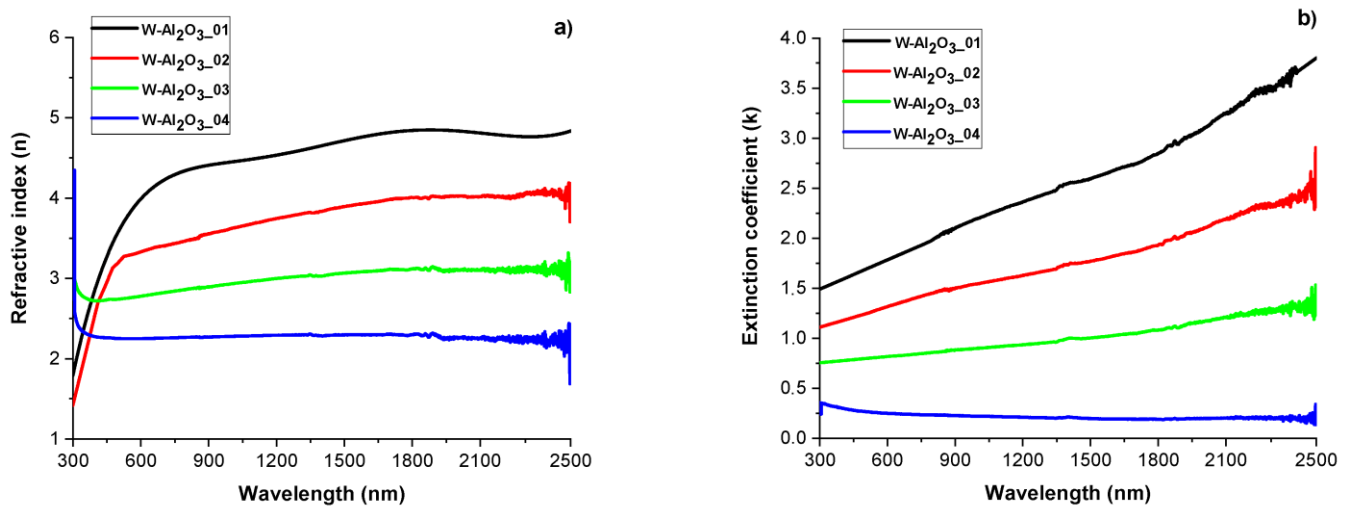


Figure 6. Transmittance (a) and reflectance (b) curves of cermet samples obtained at different power densities applied to the W target and a fixed power density applied to the Al targets.



**Figure 7.** Optical parameters of realized cermet: (a) refractive index; (b) extinction coefficient.

### 3.3. Structural Characterizations of the Realized Materials: XRD and Raman Measurements to W-O Bonds Detection

W-Al<sub>2</sub>O<sub>3</sub> samples deposited on glass and c-Si substrates were subjected to different characterizations to evaluate their structural properties and chemical composition. The oxygen gas, purposely injected into the process chamber to promote ceramic component growth, can represent the major source of degradation for the metallic component of cermet, since it can cause the oxidation of this component. Although the reactive gas was only introduced through gas rings placed around the Al targets, a certain amount of degradation of the metallic components during cermet deposition could take place. It is worth noting that the metallic component oxidation can occur in two different modes, as reported in the following:

- During the deposition of the metallic component of cermet, the plasma contains residual reactive gas coming from the region where ceramic component growth is promoted. In this case, small quantities of tungsten oxide form because of the minimal presence of oxygen;
- During the exposition of the metallic component to the plasma containing the reactive gas that promotes the ceramic component growth (this exposure is due to the rotation of the tube holder), the formation of oxides is probably limited to the W cluster boundaries, which could play a passivating function, thus limiting a further oxidation of the internal regions of clusters. Furthermore, tungsten and aluminum are simultaneously present and the latter is characterized by a redox potential less positive than that of tungsten, thus, the formation of aluminum oxide is favored nevertheless [34].

Based on these considerations, the experimental characterization focused on the structural properties of the deposited cermet samples, with particular attention on the possible presence of tungsten–oxygen bonds relative to WO<sub>3</sub> oxide. In fact, although the oxidation states for W atoms in W-Al<sub>2</sub>O<sub>3</sub> films can also be lower oxidation states (+1 to +3), the presence of WO<sub>3</sub> oxide represents the main issue for the structural stability of cermet.

X-ray diffraction patterns, shown in Figure 8a and referring to the cermet named W-Al<sub>2</sub>O<sub>3</sub>\_04, with lower metallic content than other cermet materials, were collected at an incidence angle of 3.5° to the glass substrate. This sample was obtained at the lowest power density applied to the W target; thus, it had the most W-O bonds as a percentage of the total number of bonds formed by W. Therefore, it can be expected that the W-O bonds in this sample are more easily detected than those present in other cermet samples. Hence, under the hypothesis that the compounds based on tungsten oxides (WO<sub>3</sub>) are detected inside this sample, it is reasonable to assume their presence inside other cermet materials with higher metallic content. Both “as-grown” and annealed films in vacuum ( $1 \times 10^{-3}$  Pa) at

600 °C for 6 h were characterized. The additional thermal treatment can lead to changes in the structure of films through a crystallization of the tungsten oxides, if present, which are amorphous at room temperature and when realized using the sputtering methods [35–37]. Figure 8a also shows the curve for the glass substrate used for these deposits. It was found that all films present a broad peak between 20° and 35° of 2 $\theta$ , which can be attributed to the amorphous glass substrate. No peaks due to tungsten oxides are visible, even when the glass substrate background is subtracted and the incidence angle to the sample decreased (the corresponding data are not reported).

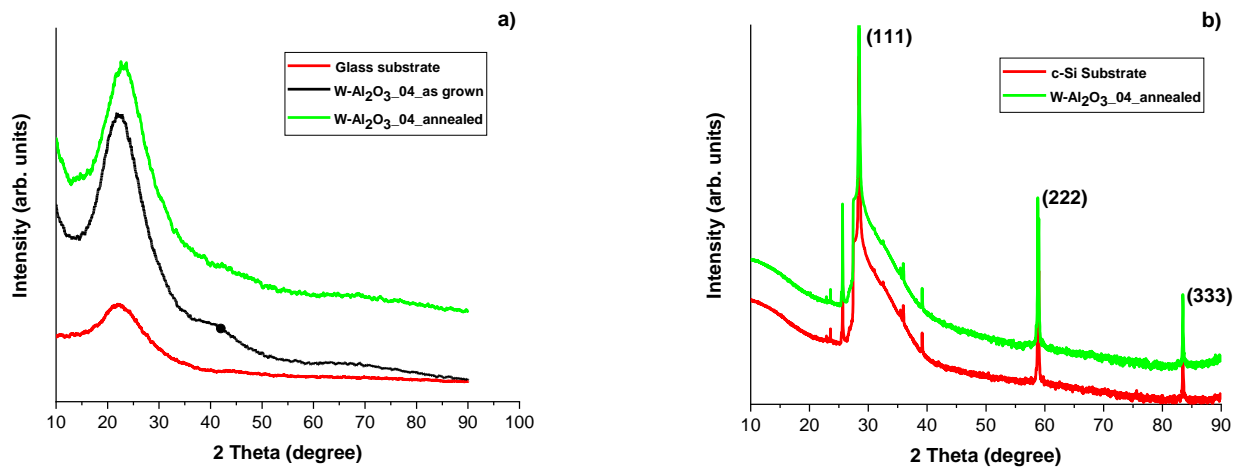


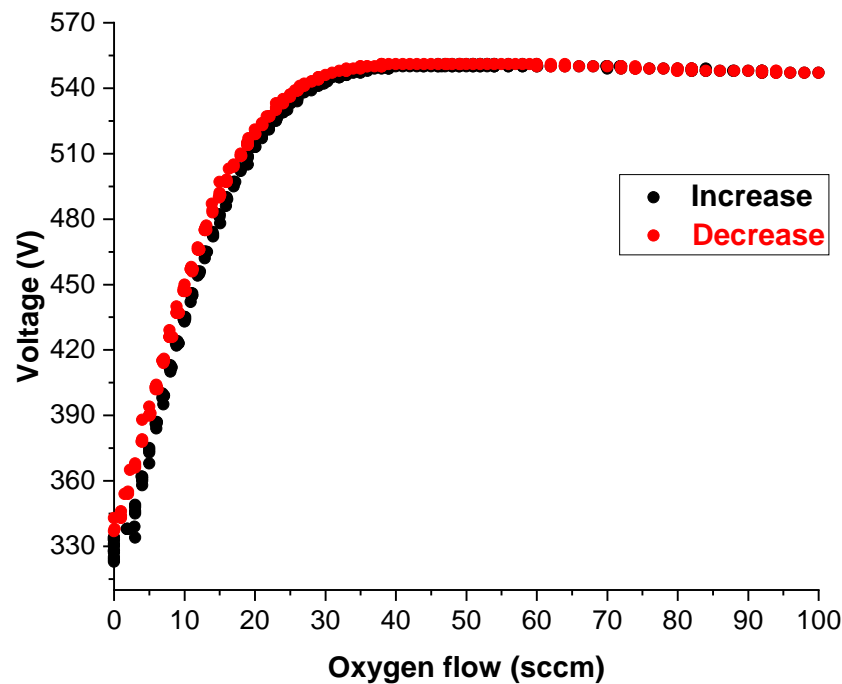
**Figure 8.** X-ray diffraction patterns of the W-Al<sub>2</sub>O<sub>3</sub>\_04 sample before and after thermal treatment, collected at an incidence angle of 3.5° to the (a) glass substrate and (b) c-Si substrate.

Since a lot of peaks relative to WO<sub>3</sub> oxide can be present in the 2 $\theta$  range of 20–35° [38], where there is also the broad peaks of the glass substrate background, the structural characterizations were also carried out on samples deposited on the c-Si substrate, to enhance the sensitivity to the thin film structure. Figure 8b shows the X-ray diffraction patterns of the W-Al<sub>2</sub>O<sub>3</sub>\_04 sample subjected to the additional thermal treatment and the used substrate. As can be seen in this case, the spectrum of thin film is very similar to that of the c-Si substrate, since it does not show peaks that can be attributed to particular compounds present in the sample. It is worth noting that some peaks visible in the spectrum are due to background noise, which are here enhanced by the logarithmic scale used to plot the obtained intensity as function of 2 $\theta$ , with the objective being to distinguish peaks attributable to the sample with respect to those of the substrate (PDF 01-075-0589).

Clearly, the film is very thin and the exiguous amount of tungsten oxides possibly present makes it very difficult to detect any peaks by XRD analysis. Moreover, at low deposition temperatures, alumina is also X-ray amorphous [39] and the stable crystalline phases are typically obtained at higher temperatures than 600 °C [40,41].

Apart from standard structural and microscopic characterizations by X-ray diffraction, other spectroscopic analytical techniques have proven to be valuable, especially for obtaining information about local structure and the chemical bonding of films. In the present work, the W-Al<sub>2</sub>O<sub>3</sub>\_04 sample was also subject to Raman spectroscopy analysis by comparing its spectrum with those of two other cermetes obtained by introducing an oxygen excess from both the Al target side (W-Al<sub>2</sub>O<sub>3</sub>\_05 sample) and the W target side (W-Al<sub>2</sub>O<sub>3</sub>\_06 sample). The aim was to deposit samples with a high number of W-O bonds and to use them as a reference for the evaluation of the presence of W-O bonds within the W-Al<sub>2</sub>O<sub>3</sub>\_04 sample under investigation. In addition, tungsten oxide samples with different chemical compositions were deposited. The reactive gas flow value was selected by monitoring the variation of cathode voltage as a function of oxygen flow injected into the process chamber, namely by manually acquiring the hysteresis curve of the W target. The appropriate oxygen flow was established to have a partially or totally poisoned target, thus

obtaining tungsten oxide samples with different chemical compositions. These samples were named WO\_01 and WO\_02, respectively, and they were used as an absolute reference to individuate W-O bonds. The evolution of cathode voltage as a function of oxygen flow is shown in Figure 9. The gradual increase of reactive gas flow leads to a gradual increase of cathode voltage up to the poisoned condition that occurs when oxygen flow is equal to 40 sccm. Under this condition, stoichiometric WO<sub>3</sub> is the major compound produced. Hence, by tuning oxygen flow between 0 and 40 sccm, the full range of W-O films with chemical compositions between pure W (corresponding to 0 sccm of O<sub>2</sub>) and trioxide tungsten WO<sub>3</sub> can be produced [42].



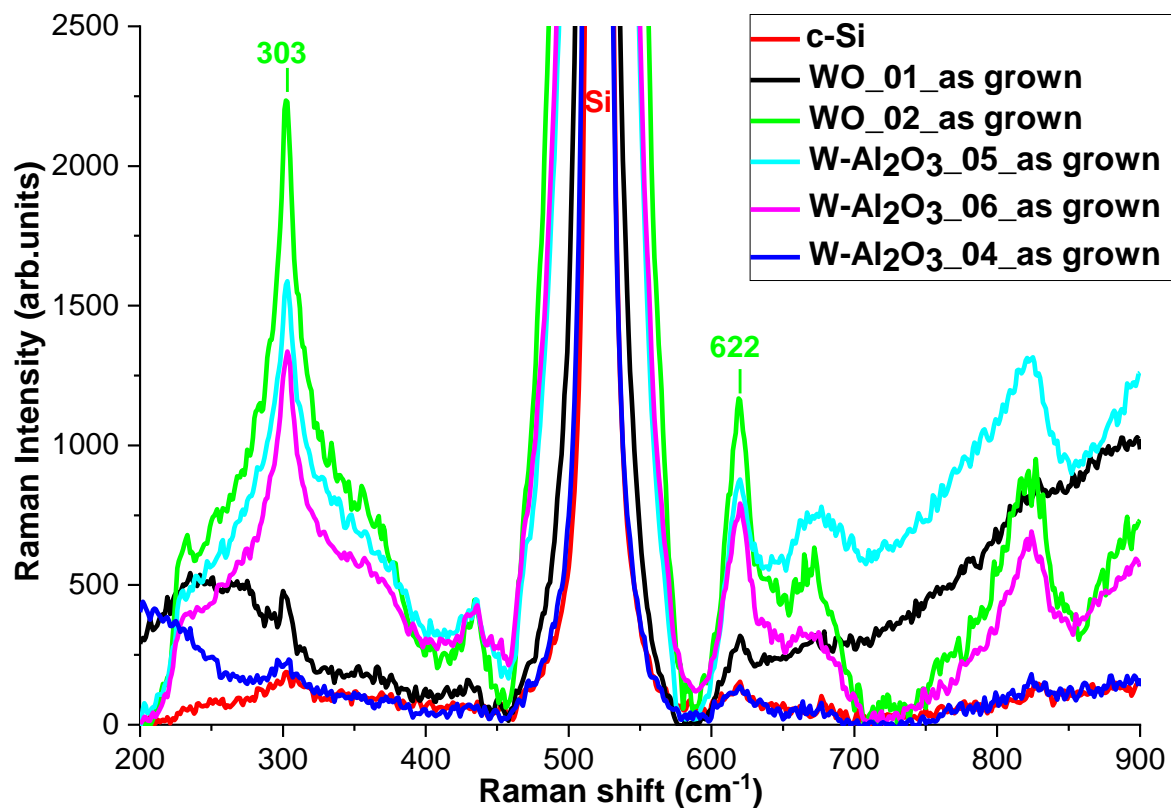
**Figure 9.** Hysteresis curve of W target manually acquired by varying oxygen gas flow.

Table 3 shows the adopted experimental conditions to deposit the above-mentioned samples, while Figure 10 shows the corresponding Raman characterizations.

**Table 3.** Process parameters adopted to deposit cermet and WO samples on c-Si substrates.

Process Parameters	W-Al <sub>2</sub> O <sub>3</sub> _04	W-Al <sub>2</sub> O <sub>3</sub> _05	W-Al <sub>2</sub> O <sub>3</sub> _06	WO_01	WO_02
Argon flow (sccm)	400	400	400	400	400
Oxygen flow (sccm)	5.4 (PEM)	19 (Al side)	19 (Al side) + 35 (W side)	12 (W side)	40 (W side)
Process pressure (Pa)	~1	~1	~1	~1	~1
Al power density (W/cm <sup>2</sup> )	1.84	1.84	1.84	/	/
W power density (W/cm <sup>2</sup> )	1.33	1.33	1.33	1.33	1.33

The Raman spectrum of the pure silicon is also shown in this figure, both for an easier comparison and for assignment of the features at 303 cm<sup>-1</sup> and 622 cm<sup>-1</sup> to the presence of Si-O bonds [43]. Samples named WO\_02, W-Al<sub>2</sub>O<sub>3</sub>\_05, and W-Al<sub>2</sub>O<sub>3</sub>\_06 have two broad bands around 200–400 cm<sup>-1</sup> and 700–850 cm<sup>-1</sup>; these are the result of weak peak combination due to vibration modes of the W-O bond and reveal the amorphous nature of these samples [44]. Furthermore, the spectrum of the W-Al<sub>2</sub>O<sub>3</sub>\_04 sample is very similar to the c-Si spectrum, since it does not show the characteristic peaks associated with the vibration modes of the W-O bond.



**Figure 10.** Comparison between Raman spectra of cermet and WO samples deposited on c-Si substrate by varying reactive gas flow.

The sharpening and increasing of these peaks' intensities, which become more evident at high temperature (600 °C for 6 h in vacuum), demonstrate a trend toward ordering, that is, toward the presence of crystalline domains. This behavior is reported in Figure 11. The Raman spectrum of the WO\_01 sample is intense and detailed with Raman lines at 284 cm<sup>-1</sup> (s), 333 cm<sup>-1</sup> (w), 348 cm<sup>-1</sup> (w), 423 cm<sup>-1</sup> (w), 482 cm<sup>-1</sup> (m), 599 cm<sup>-1</sup> (m), 617 cm<sup>-1</sup> (m), and 782 cm<sup>-1</sup> (vs) which shift to higher energies (w-weak; m-medium; s-strong; vs-very strong). This spectrum is attributed to the WO<sub>2</sub> rutile structure [45,46].

However, thermal annealing treatments only promoted the crystallization of the WO\_01 sample, while the other samples still had an amorphous nature but with more intensive broad bands. All cermet materials had a shift of broad peak at 700–850 cm<sup>-1</sup> towards the new Raman shift value of 810 cm<sup>-1</sup>, corresponding to the LO vibration mode of the W-O-W bond of the  $\gamma$ -WO<sub>3</sub> monoclinic structure [47]. This phenomenon is probably due to a rearrangement of atom groups favored by high annealing temperature. Furthermore, the Raman spectrum of the W-Al<sub>2</sub>O<sub>3</sub>\_04 sample shows some modifications with respect to c-Si spectrum, with the characteristic peak around 810 cm<sup>-1</sup> of the W-O bond. Nevertheless, its intensity is very low, as the presence of W-O bonds is almost negligible, and therefore does not compromise the structural stability of the cermet at the selected operating conditions. Lastly, it is worth noting that the absence of crystallization for the WO\_02 sample can be attributed to an oxygen deficit within the structure that does not allow for the formation of the monoclinic structure of  $\gamma$ -WO<sub>3</sub>. Hence, the sample was subjected to a thermal annealing process at 600 °C in air. Raman analysis performed after this treatment revealed the formation of the monoclinic structure of  $\gamma$ -WO<sub>3</sub>, distinguished by the following characteristic peaks: 268 cm<sup>-1</sup>, 714 cm<sup>-1</sup>, and 810 cm<sup>-1</sup>, as reported in Figure 12 [38,43–46].

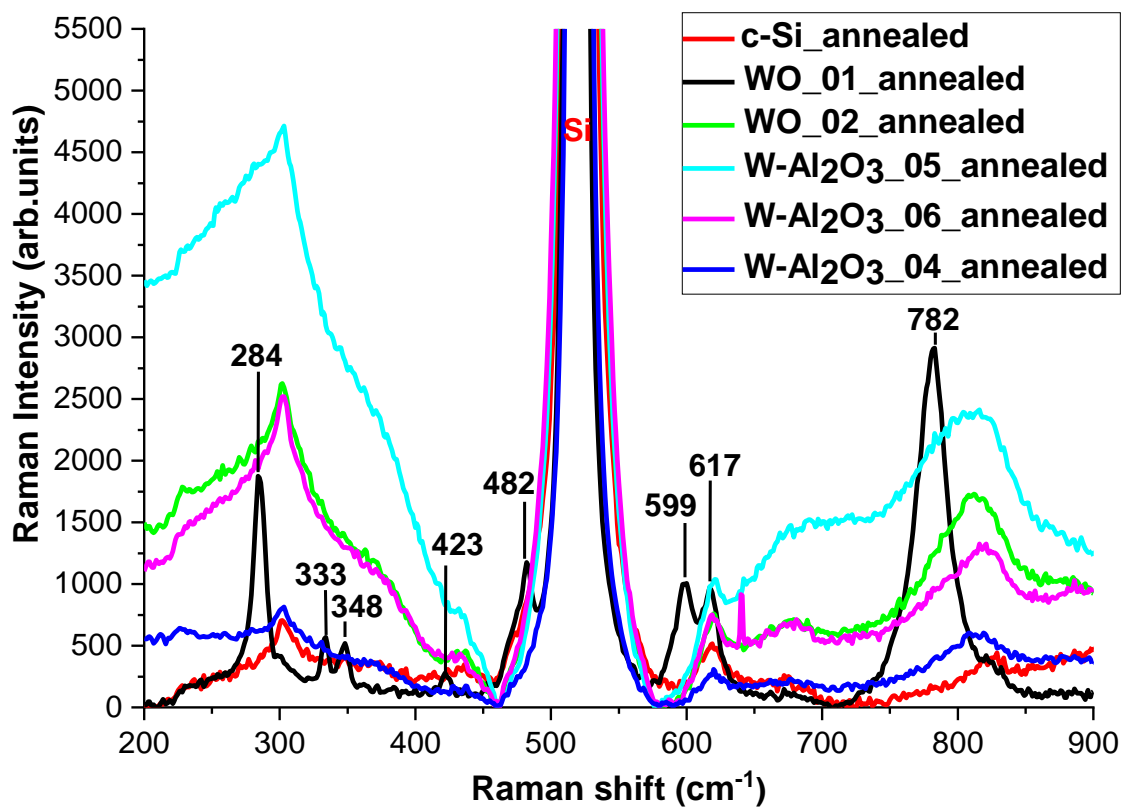


Figure 11. Comparison between Raman spectra of cermet and WO samples deposited on c-Si substrate by varying reactive gas flow and subsection to thermal annealing treatment in vacuum at 600 °C for 6 h.

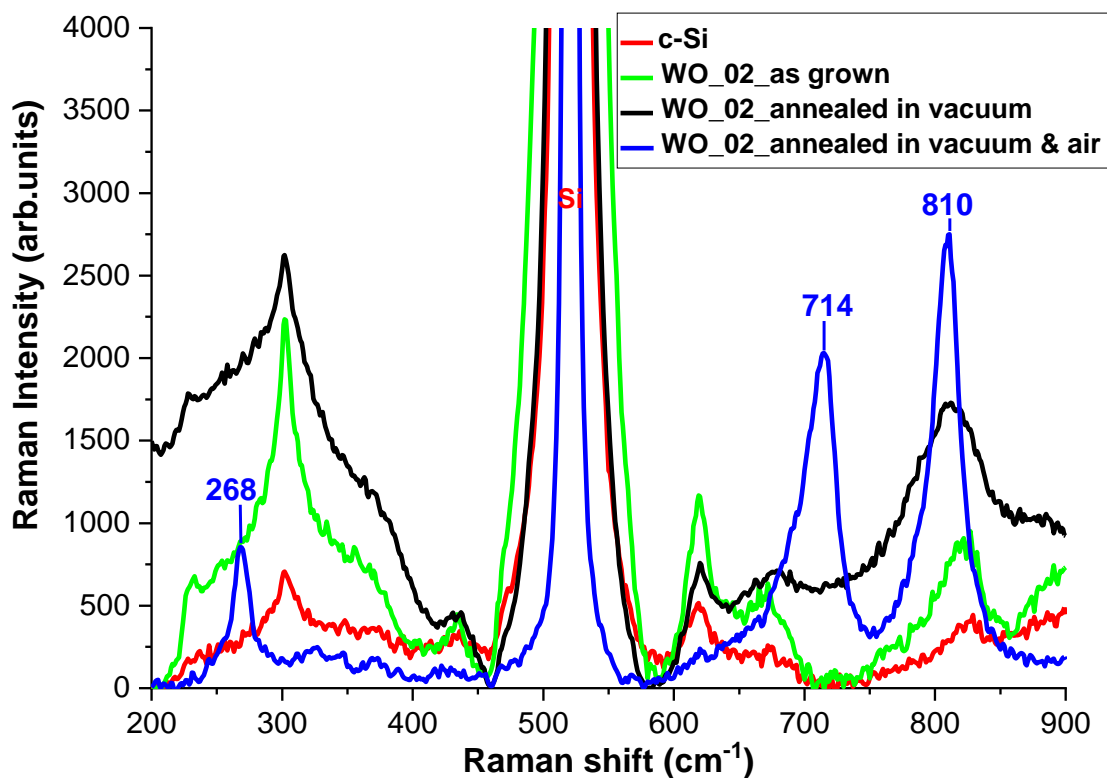
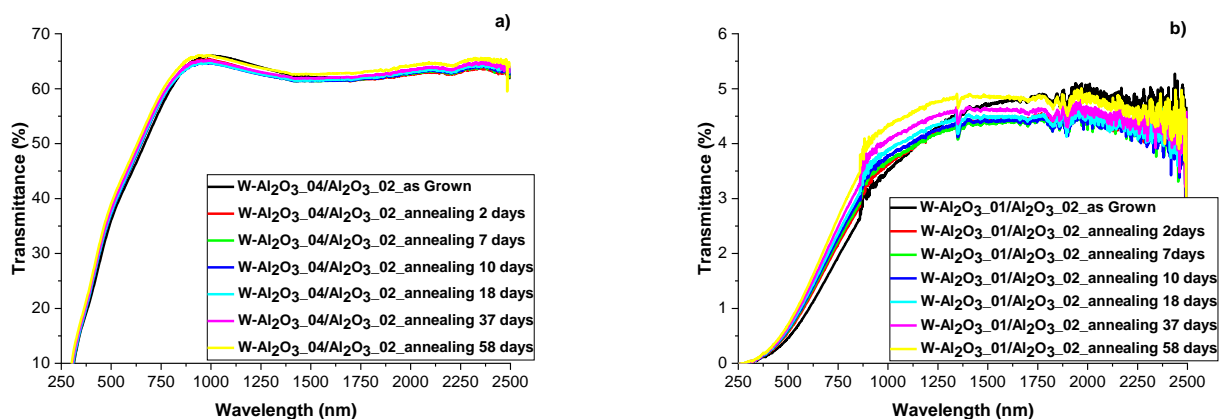


Figure 12. Comparison between Raman spectra obtained on as-grown WO<sub>02</sub> and the annealed sample.

### 3.4. Evaluation of Optical and Structural Stability of Materials through Annealing Tests

The evaluations of the optical and structural stability of realized materials were carried out by subjecting the samples to heat treatments in a programmable oven operating under vacuum ( $1 \times 10^{-3}$  Pa) at a temperature of  $620^\circ\text{C}$ . The details of these annealing cycles are reported in the Section 2. In order to simulate the real operating conditions of the materials comprising the selective coatings of solar receivers, two samples with double layer structures were realized. These samples first have a cermet layer, which is different in terms of metallic content, followed by the same alumina layer. Since solar coatings are characterized by an external antireflection layer that protects the internal layers, the realized structures are able to reproduce the real operative conditions of cermet because they simulate the solar coating structure effectively. In detail, the first sample, named Bilayer\_01, is characterized by a cermet layer with the lowest metallic content and was realized by adopting the same experimental conditions as the W-Al<sub>2</sub>O<sub>3</sub>\_04 sample. The second sample, named Bilayer\_02, had a cermet layer with the highest metallic content and was deposited by adopting the same experimental conditions as the W-Al<sub>2</sub>O<sub>3</sub>\_01 sample. Therefore, these samples were representative of the extreme conditions of the realization of graded cermet within solar coatings. The alumina top layer was realized by adopting the experimental conditions of the Al<sub>2</sub>O<sub>3</sub>\_02 sample. Both structures were characterized by a bottom cermet layer of 100 nm and a top ceramic layer of 100 nm.

Spectrophotometric analyses were performed on the samples “as-grown” and on the samples after each annealing cycle. Figure 13a,b and Figure 14a,b show the transmittance and reflectance curves of these samples, respectively.



**Figure 13.** Comparison between the transmittance curves of as-grown and annealed samples: (a) Bilayer\_01, (b) Bilayer\_02.

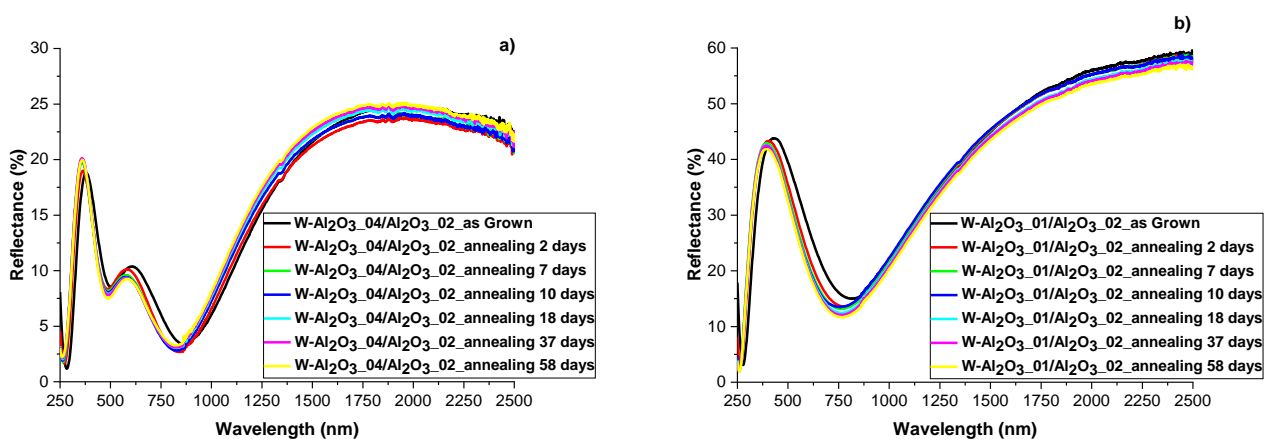


**Figure 14.** Comparison between the reflectance curves of as-grown and annealed samples: (a) Bilayer\_01, (b) Bilayer\_02.

The transmittance and reflectance curves in Figure 13a,b and Figure 14a,b show little to negligible variations between the as-grown and annealed samples, clearly indicating the high optical and structural stability of these bi-layer structures. In conclusion, these materials can be considered stable under vacuum at 620 °C.

#### 4. Conclusions

The experimental activity described in this work concerns the realization of ceramic and cermet materials characterized by high structural and chemical stability under vacuum and at high temperature and obtained through the optimization of high-deposition-rate processes.

Particularly, the “dual magnetron” reactive sputtering in transition mode with MF power supply was the technique employed to deposit the ceramic materials, namely alumina. This material was employed both as an antireflection layer and as a ceramic component of the optical absorber layer. In order to deposit ceramic materials with stable optical and structural properties independently from the production processes, a PEM control system was used. The optimized reactive sputtering process in transition mode showed a deposition rate about sixteen times higher than that of the reactive sputtering in poisoned mode. In addition, a repeatable and stable process was developed.

Regarding the cermet deposition, the reactive co-sputtering technique in transition regime was implemented to deposit ceramic (alumina) and metallic (tungsten) components concurrently. Samples characterized by a strongly variable extinction coefficient and a suitable thickness were obtained; these characteristics are very useful, since they allow one to realize a solar absorber with a graded metallic profile, namely cermet layers in which the metallic content decreases from infrared back reflector to antireflection filter. This type of structure ensures good absorption of incoming solar radiation.

The investigation into the stability of realized cermet was carried out by means of several material characterization methods before and after the annealing process in vacuum at high temperature. In particular, the structural analysis, such as Raman spectroscopy, allowed for the individuation of peaks corresponding to the WO<sub>3</sub> compound. This compound is a volatile oxide at the operative conditions of the receiver tube and therefore could damage the structural stability of cermet. However, it was found that the intensity of these peaks was very low, since the presence of W-O bonds was almost negligible, and therefore did not compromise the structural stability of the cermet at the selected operating conditions. In addition, the spectrophotometric analysis for optical and chemical structural stability showed negligible variations between the as-deposited and annealed samples, clearly indicating the optimal optical and structural stability of samples realized through reactive magnetron sputtering technique in transition mode.

**Author Contributions:** Conceptualization, C.D., A.D., S.E. and A.G.; methodology, C.D., A.D., S.E. and A.G.; software, A.D. and S.E.; validation, C.D., A.D., S.E. and A.G.; formal analysis, C.D., A.D., S.E. and A.G.; investigation, C.D., A.D., S.E., A.G. and D.M.G.; resources, A.G.; data curation, C.D., A.D. and S.E.; writing—original draft preparation, C.D.; writing—review and editing, C.D., A.D., S.E., A.G., D.M.G. and M.L.; visualization, C.D., A.D., S.E. and A.G.; supervision, M.L. All authors have read and agreed to the published version of the manuscript.

**Funding:** This research received no external funding.

**Institutional Review Board Statement:** Not applicable.

**Informed Consent Statement:** Not applicable.

**Data Availability Statement:** Not applicable.

**Acknowledgments:** The results presented in this paper have been obtained under the framework of the project “Concentrating Solar Power,” as part of the “Electric System Research” Program 2019–2021, with the financial support of Italian Ministry for Ecological Transition.

**Conflicts of Interest:** The authors declare no conflict of interest.

## References

1. Selvakumar, N.; Barshilia, H.C. Review of physical vapor deposited (PVD) spectrally selective coatings for mid- and high-temperature solar thermal applications. *Sol. Energy Mater. Sol. Cells* **2012**, *98*, 1–23. [CrossRef]
2. Bello, M.; Shanmugan, S. Achievements in mid and high-temperature selective absorber coatings by physical vapor deposition (PVD) for solar thermal Application—A review. *J. Alloys Compd.* **2020**, *839*, 155510. [CrossRef]
3. Noc, L.; Jerman, I. Review of the spectrally selective (CSP) absorber coatings, suitable for use in SHIP. *Sol. Energy Mater. Sol. Cells* **2022**, *238*, 111625. [CrossRef]
4. Ritchie, I.T.; Window, B. Applications of thin graded-index films to solar absorbers. *Appl. Opt.* **1977**, *16*, 1438–1443. [CrossRef]
5. Sathiaraj, T.S.; Thangaraj, R.; Alsharbaty, H.; Bhatnagar, M.; Agnihotri, O.P. Ni-Al<sub>2</sub>O<sub>3</sub> Selective Cermet Coatings for photothermal conversion up to 500 °C. *Thin Solid Film.* **1990**, *190*, 241–254. [CrossRef]
6. Barshilia, H.C.; Kumar, P.K.; Rajam, S.; Biswas, A. Structure and optical properties of Ag–Al<sub>2</sub>O<sub>3</sub> nanocermet solar selective coatings prepared using unbalanced magnetron sputtering. *Sol. Energy Mater. Sol. Cells* **2011**, *95*, 1707–1715. [CrossRef]
7. Xinkang, D.; Cong, W.; Tianmin, W.; Long, Z.; Bulia, C. Microstructure and spectral selectivity of Mo-Al<sub>2</sub>O<sub>3</sub> solar selective absorbing coatings after annealing. *Thin Solid Films* **2008**, *516*, 3971–3977. [CrossRef]
8. Cheng, J.; Wang, C.; Wang, W.; Du, X.; Liu, Y.; Xue, Y. Improvement of thermal stability in the solar selective absorbing Mo–Al<sub>2</sub>O<sub>3</sub> coating. *Sol. Energy Mater. Sol. Cells* **2013**, *109*, 204–208. [CrossRef]
9. Tsegay, M.; Gebretinsae, H.; Sackey, J.; Arendse, C.; Nuru, Z. Structural and optical properties of Pt-Al<sub>2</sub>O<sub>3</sub> double cermet as selective solar absorber. *Mat. Today: Proc.* **2021**, *36*, 571–575. [CrossRef]
10. Chevaprak, T.; Chomcharoen, N.; Techapiesancharoenkij, R.; Kumnorkaew, P.; Muangnapoh, T.; Surawathanawises, K. Solution-based Ni-Al<sub>2</sub>O<sub>3</sub> Solar Selective Coating using Convective Deposition. *Mater. Today: Proc.* **2020**, *23*, 745–751. [CrossRef]
11. Antonaia, A.; Castaldo, A.; Addonizio, M.L.; Esposito, S. Stability of W-Al<sub>2</sub>O<sub>3</sub> cermet based solar coating for receiver tube operating at high temperature. *Sol. Energy Mater. Sol. Cells* **2010**, *94*, 1604–1611. [CrossRef]
12. Rebouta, L.; Sousa, A.; Capela, P.; Andritschky, M.; Santilli, P.; Matilainen, A.; Pischow, K.; Barradas, N.P.; Alves, E. Solar selective absorbers based on Al<sub>2</sub>O<sub>3</sub>:W cermets and AlSiN/AlSiON layers. *Sol. Energy Mater. Sol. Cells* **2015**, *137*, 93–100. [CrossRef]
13. Zhou, J.; Li, S.; Yu, Y. First principle calculation of thermal conversion properties of W-Al<sub>2</sub>O<sub>3</sub> based solar selective absorbing coating. *Comput. Mater. Sci.* **2022**, *211*, 111501. [CrossRef]
14. Kathrein, M.; Schintlmeister, W.; Wallgram, W.; Schleinkofe, U. Doped CVD Al<sub>2</sub>O<sub>3</sub> coatings for high performance cutting tools. *Surf. Coat. Technol.* **2003**, *163–164*, 181–188. [CrossRef]
15. Mohammed, A.; Khodair, Z.T.; Khadom, A.A. Preparation, characterization and application of Al<sub>2</sub>O<sub>3</sub> nanoparticles for the protection of boiler steel tubes from high temperature corrosion. *Ceram. Int.* **2020**, *46*, 26945–26955.
16. Antonaia, A.; Esposito, S.; Addonizio, M.L.; Guglielmo, A. Solar Selective Absorber on Double Nitride Composite Material and Process for Its Preparation. Italy Patent IPNWO/2012/172505, 20 December 2012.
17. MATS Project. Available online: <http://www.mats.enea.it> (accessed on 7 September 2021).
18. Schiller, S.; Goedicke, K.; Reschke, J.; Kirchhoff, V.; Schneider, S.; Milde, F. Pulsed magnetron sputter technology. *Surf. Coat. Technol.* **1993**, *61*, 331–337. [CrossRef]
19. Fietzke, F.; Goedicke, K.; Hempel, W. The deposition of hard crystalline Al<sub>2</sub>O<sub>3</sub> layers by means of bipolar pulsed magnetron sputtering. *Surf. Coat. Technol.* **1996**, *286–287*, 657–663. [CrossRef]
20. Musil, J.; Baroch, P.; Vlček, J.; Nam, K.; Han, J.G. Reactive magnetron sputtering of thin films: Present status and trends. *Thin Solid Films* **2005**, *475*, 208–218. [CrossRef]
21. Madsen, N.; Christensen, B.H.; Louring, S.; Berthelsen, A.N.; Almqvist, K.P.; Nielsen, L.P.; Bøttiger, J. Controlling the deposition rate during target erosion in reactive pulsed DC magnetron sputter deposition of alumina. *Surf. Coat. Technol.* **2012**, *206*, 4850–4854. [CrossRef]
22. Carreri, F.C.; Bandorf, R.; Gerdes, H.; Vergöhl, M.; Bräuer, G. Highly insulating alumina films by a bipolar reactive MF sputtering process with special arc handling. *Surf. Coat. Technol.* **2016**, *290*, 82–86. [CrossRef]
23. Wallin, E.; Helmersson, U. Hysteresis-free reactive high power impulse magnetron sputtering. *Thin Solid Films* **2008**, *516*, 6398–6401. [CrossRef]
24. Safi, I. Recent aspects concerning DC reactive magnetron sputtering of thin films: A review. *Surf. Coat. Technol.* **2000**, *27*, 203–218. [CrossRef]
25. Becerril-Gonzalez, J.J.; Castro-Chong, A.M.; Oskam, G.; Arés-Muz, O. Sputter deposition of Mo-alumina cermet solar selective coatings: Interrelation between residual oxygen incorporation, structure and optical properties. *Mater. Res. Express* **2021**, *8*, 105506. [CrossRef]
26. Esposito, S.; D'Angelo, A.; Diletto, C.; Guglielmo, A.; Lanchi, M.; Rossi, G. Solar Coatings Based on Ag Infrared Reflector with High Stability at Medium and High Temperature. *Energies* **2021**, *14*, 5910. [CrossRef]
27. D'Angelo, A.; Diletto, C.; Esposito, S.; Graditi, G.; Guglielmo, A.; Lanchi, M.; Rossi, G. Spectrally selective solar coating based on W-AlN cermet fabricated by reactive sputtering processes at high deposition rate. *AIP Conf. Proc.* **2022**, *2445*, 020002.
28. Takenaka, K.; Setsuhara, Y.J.; Han, G.; Uchida, G.; Ebe, A. High-rate deposition of silicon nitride thin films using plasma-assisted reactive sputter deposition. *Thin Solid Films* **2019**, *685*, 306–311. [CrossRef]
29. Cheng, Y.H.; Lee, P.I.; Sakalley, S.; Wen, C.K.; Cheng, W.C.; Sun, H.; Chen, S.C. Enhanced Electrical Properties of Copper Nitride Films Deposited via High Power Impulse Magnetron Sputtering. *Nanomaterials* **2022**, *12*, 2814. [CrossRef]

30. Nadel, S.J.; Greene, P.; Rietzel, J.; Strümpfel, J. Equipment, materials and processes: A review of high rate sputtering technology for glass coating. *Thin Solid Films* **2003**, *442*, 11–14. [[CrossRef](#)]
31. Blackburn, P.E.; Hoch, M.; Johnston, H. The vaporization of Molybdenum and Tungsten Oxides. *J. Phys. Chem.* **1958**, *62*, 769–773. [[CrossRef](#)]
32. Gulbransen, E.A.; Andrew, K.F. Kinetics of the Oxidation of Pure Tungsten from 500 °C to 1300 °C. *J. Electrochem. Soc.* **1960**, *107*, 619–628. [[CrossRef](#)]
33. De Sio, A.; Madena, T.; Huber, R.; Parisi, J.; Neyshtadt, S.; Deshler, F.; Da Como, E.; Esposito, S.; Von Hauff, E. Solvent additives for tuning the photovoltaic properties of polymer–fullerene solar cells. *Sol. Energy Mater. Sol. Cells* **2011**, *95*, 3536–3542. [[CrossRef](#)]
34. Kuckelkorn, T.; Graf, W.; Hildebrandt, C.; Georg, A. Radiation Selective Absorber Coating for an Absorber Pipe, Absorber Pipe with Said Coating, and Method of Making Same. US Patent US7,909,029 B2, 27 November 2006.
35. Romanyuk, A.; Oelhafen, P. Evidence of different oxygen states during thermal coloration of tungsten oxide. *Sol. Energy Mater. Sol. Cells* **2006**, *90*, 1945–1950. [[CrossRef](#)]
36. Maffei, T.G.; Yung, D.; LePennec, L.; Penny, M.W.; Cobley, R.J.; Comini, E.; Sberveglieri, G.; Wilks, S.P. STM and XPS characterisation of vacuum annealed nanocrystalline WO<sub>3</sub> films. *Surf. Sci.* **2007**, *601*, 4953–4957. [[CrossRef](#)]
37. Maffei, T.G.; Penny, M.W.; Cobley, R.J.; Comini, E.; Sberveglieri, G.; Wilks, S.P. XPS Characterisation of vacuum annealed nanocrystalline WO<sub>3</sub> films. *e-J. Surf. Sci. Nanotechnol.* **2009**, *7*, 319–322. [[CrossRef](#)]
38. Shapovalov, V.I.; Lapshin, A.E.; Gagarin, A.G.; Efimenko, L.P. Chemical composition and crystal structure of tungsten oxide films. *Glass Phys. Chem.* **2014**, *40*, 553–569. [[CrossRef](#)]
39. Chou, T.C.; Adamson, D.; Mardinly, J.; Nieh, T.G. Microstructural evolution and properties of nanocrystalline alumina made by reactive sputtering deposition. *Thin Solid Film.* **1991**, *205*, 131–139. [[CrossRef](#)]
40. Musil, J.; Blažek, J.; Zeman, P.; Prokšová, Š.; Šašek, M.; Čerstvý, R. Thermal stability of alumina thin films containing  $\gamma$ -Al<sub>2</sub>O<sub>3</sub> phase prepared by reactive magnetron sputtering. *Appl. Surf. Sci.* **2010**, *257*, 1058–1062. [[CrossRef](#)]
41. Edlmayr, V.; Moser, M.; Walter, C.; Mitterer, C. Thermal stability of sputtered Al<sub>2</sub>O<sub>3</sub> coatings. *Surf. Coat. Technol.* **2010**, *204*, 1576–1581. [[CrossRef](#)]
42. Parreira, N.M.; Carvalho, N.J.; Cavaleiro, A. Synthesis, structural and mechanical characterization of sputtered tungsten oxide coatings. *Thin Solid Films* **2006**, *510*, 191–196. [[CrossRef](#)]
43. Manciu, F.S.; Enriquez, J.L.; Durrer, W.G.; Yun, Y. Spectroscopic analysis of tungsten oxide thin films. *J. Mater. Res.* **2010**, *25*, 2401–2406. [[CrossRef](#)]
44. Besozzi, E.; Dellasega, D.; Russo, V.; Conti, C.; Passoni, M.; Beghi, M.G. Thermomechanical properties of amorphous metallic tungsten-oxygen and tungsten-oxide coatings. *Mater. Des.* **2019**, *165*, 107565. [[CrossRef](#)]
45. Frey, G.L.; Rothschild, A.; Sloan, J.; Rosentsveig, R.; Popovitz-Biro, R.; Tenne, R. Investigations of Nonstoichiometric Tungsten Oxide Nanoparticles. *J. Solid State Chem.* **2001**, *162*, 300–314. [[CrossRef](#)]
46. Kumar, V.B.; Mohanta, D. Formation of nanoscale tungsten oxide structures and colouration characteristics. *Bull. Mater. Sci.* **2011**, *34*, 435–442.
47. Daniel, M.F.; Desbat, B.; Lassegue, J. Infrared and Raman Study of WO<sub>3</sub> Tungsten Trioxide and WO<sub>3</sub>xH<sub>2</sub>O Tungsten Trioxide Hydrates. *J. Solid State Chem.* **1987**, *67*, 235–247. [[CrossRef](#)]

**Disclaimer/Publisher’s Note:** The statements, opinions and data contained in all publications are solely those of the individual author(s) and contributor(s) and not of MDPI and/or the editor(s). MDPI and/or the editor(s) disclaim responsibility for any injury to people or property resulting from any ideas, methods, instructions or products referred to in the content.